International Journal of Biological Macromolecules 316 (2025) 144466

Contents lists available at ScienceDirect

International Journal of Biological Macromolecules

journal homepage: www.elsevier.com/locate/ijbiomac

Optimization of 3D-printed bio-based super tough PLA (ST-PLA) scaffolds for cancellous bone regeneration: mechanical properties, lattice architecture, and osseointegration potential

Ray Tahir Mushtaq [a,1], Ghulam Hassan Askari [a], Chengwei Bao [a,b], Yanen Wang [a,*,1], Khubab Ahmed [c], Aqib Mashood Khan [d,*], Shubham Sharma [e,f,g,**], Mohammed Alkahtani [h]

[a] Bio-Additive Manufacturing University-Enterprise Joint Research Center of Shaanxi Province, Department of Industry Engineering, Northwestern Polytechnical University, Xi'an 710072, China
[b] School of Intelligent Manufacturing and Control Technology, Xi'an Mingde Institute of Technology, Xi'an 710124, China
[c] Binjiang Institute of Artificial Intelligence, Zhejiang University of Technology, Hangzhou 310051, Zhejiang, China
[d] College of Mechanical and Electrical Engineering, Nanjing University of Aeronautics and Astronautics, Nanjing 210016, China
[e] Department of Technical Sciences, Western Caspian University, Baku, Azerbaijan
[f] Centre for Research Impact and Outcome, Chitkara University Institute of Engineering and Technology, Chitkara University, Rajpura 140401, Punjab, India
[g] Jadara University Research Center, Jadara University, Jordan
[h] Department of Industrial Engineering, College of Engineering, King Saud University, P.O. Box 800, Riyadh 12372, Saudi Arabia

ARTICLE INFO

Keywords:
Fused filament fabrication (FFF)
Super tough polylactic acid (ST-PLA)
Cancellous bone implants
Surface roughness
Compressive strength
3D printing optimization

ABSTRACT

Cancellous bone implants require materials that not only exhibit adequate mechanical strength but also possess suitable elasticity to minimize stress shielding and ensure efficient osseointegration. This study addresses these challenges by optimizing the 3D printing parameters and cellular lattice configurations of Super Tough Polylactic Acid (ST-PLA), targeting improved mechanical properties and suitability for cancellous bone regeneration. The optimization process employed Response Surface Methodology (RSM) in combination with a multi-input, multi-output (MIMO) predictive model, with a Box-Behnken Design (BBD) utilized to assess the effects of layer thickness, print speed, and cellular wall thickness across 17 experimental conditions. The results demonstrated a compressive strength range from 0.25 MPa to 1.41 MPa, with an optimal predicted strength of 1.38 MPa. Surface roughness was found to be 6.98 μm (Sa) and 8.38 μm (Sq), suitable for enhancing osseointegration. The elastic modulus of the fabricated ST-PLA scaffolds was measured at 0.075 GPa, which is remarkably close to the lower range of human cancellous bone (0.1–0.5 GPa), significantly reducing the potential for stress shielding. Compared to previous studies, this work showed approximately 28 % improvement in compressive strength and around 25 % improvement in getting near cancellous bone elastic modulus, highlighting the potential of ST-PLA scaffolds as a viable solution for bone grafting. Scanning Electron Microscopy (SEM) confirmed the optimized lattice structures exhibited reduced porosity, minimized microstructural defects, and improved interlayer bonding, ensuring enhanced mechanical integrity. These findings demonstrate that ST-PLA scaffolds offer a promising balance between mechanical performance, surface finish, and compliance, making them ideal candidates for biomedical implants. This work not only advances the design of bone grafting materials but also has significant clinical applications for improving surgical outcomes and accelerating patient recovery.

---

* Corresponding authors.

** Correspondence to: S. Sharma, Department of Technical Sciences, Western Caspian University, Baku, Azerbaijan.

E-mail addresses: tahirmushtaqray@mail.nwpu.edu.cn (R.T. Mushtaq), engrghulamhassanaskari@mail.nwpu.edu.cn (G.H. Askari), baocw@mail.nwpu.edu.cn (C. Bao), wangyanen@126.com (Y. Wang), dr.aqib@nuaa.edu.cn (A.M. Khan), shubham543sharma@gmail.com, shubhamsharmacsirclri@gmail.com (S. Sharma), moalkahtani@ksu.edu.sa (M. Alkahtani).

[1] Yanen Wang has participated equally in the manuscript, so, he should be considered as Co-first author.

https://doi.org/10.1016/j.ijbiomac.2025.144466
Received 9 March 2025; Received in revised form 3 May 2025; Accepted 19 May 2025

1. Introduction

Cancellous bone grafting is an important surgical intervention when an injury, a congenital disability, or a disease has compromised the structural integrity or regenerative capacity of bones, particularly in regions requiring porosity and vascularization [1]. It is essential for restoring those with impaired mastication, speech, respiration, and aesthetic improvement related to psychological well-being. In cancellous bone grafting, the materials must have a unique combination of mechanical strength, biocompatibility, and the ability to integrate well with the surrounding bony tissues [2]. Due to the complex anatomy of the cancellous region, wherein high functionality is demanded from these bones, developing appropriate bone graft materials becomes paramount [3,4].

In recent years, 3D printing has provided new frontiers in cancellous reconstruction. It allows one to fabricate patient-specific implants and scaffolds with precision and conformation to the intricate anatomy [5]. Additive manufacturing (AM) builds parts in layers from an electronic model capable of making complex structures [6,7] similar to the natural architecture of bone. Mojaver et al. [8] explored innovative auxetic megastructures fabricated from thermoplastic polyurethane, highlighting their enhanced deformation and load-distribution capabilities. Such advancements demonstrate the potential of these structures in achieving tailored mechanical properties for biomedical applications. Among different AM techniques, Fused Filament Fabrication (FFF) is the most widely used, especially for providing a thorough account of processing in the case of polymer-based materials such as Polylactic Acid (PLA) [9–11]. PLA is one of the most preferred biomaterials due to its biodegradable nature, easy processing, and good mechanical properties that make it suitable for biomedical applications [12].

PLA is a polymer derived from renewable resources, which has become a benchmark material in 3D printing for biomedical uses due to its biocompatibility and ease of use. However, at standard conditions [13], PLA presents mechanical strength issues, especially in load-bearing applications. Nevertheless, several enhanced variants were produced to overcome such limitations: for example, the Super-Tough Polylactic acid (ST-PLA), featuring improved toughness and flexibility properties highly wanted in cancellous applications because of the dynamic mechanical stress's implants have to resist [14]. Further development in porous lattice structures has extended their application areas into bone grafting. The design of these structures aims to mimic natural bone's porosity, providing scaffolds that support mechanical loads and help in tissue ingrowth and vascularization [15]. Aghaiee et al. [16] combined 3D printing with gas foaming to create hierarchical scaffolds that effectively balance porosity and mechanical strength, optimizing the conditions for bone tissue engineering applications. Their findings highlight the importance of multi-objective optimization for scaffold design in cancellous reconstruction. Recent studies have demonstrated the potential of PLA-based composites with bioactive reinforcements like Mg and TCP for enhanced mechanical strength, osseointegration, and antibacterial properties [17–19]. These advancements highlight the promise of ST-PLA scaffolds in orthopaedic and wound healing applications, warranting further bio-functionalization to improve clinical performance.

One of the areas most investigated when performing 3D printing in porous scaffolds is bone grafting. Cox et al. [20] demonstrated that PLA scaffolds with controlled porosity can have compressive strengths as low as 0.88 MPa, depending on the structural design and porosity level. This study again shows that structural design features meet the desired mechanical properties for specific applications. Hassanajili et al. [21] further expanded on this by optimizing PLA-based scaffolds with composite materials to obtain compressive strengths suitable for low-load-bearing applications, such as cancellous reconstruction. Their findings underline the importance of material composition in determining the mechanical performance of scaffolds. Dussault et al. [22] showed that PLLA scaffolds fabricated for bone defect repair can be fabricated to achieve selected mechanical properties. This focuses on optimizing structures to balance mechanical performance and biological functionality. In addition, Hasanzadeh [23] utilized machine learning algorithms to optimize hybrid auxetic structures fabricated through FFF, achieving significant improvements in energy absorption and compressive strength. These contributions emphasize the transformative role of computational techniques in scaffold design for biomedical applications. Until now, much advancement has been done in scaffold construction; the main challenges remain in ensuring that scaffold designs meet the load-bearing requirements of the region of interest and provide adequate porosity to allow appropriate tissue integration. Table 1 has depicted the overview of the existing literature evaluations of the present study and comparable research.

The challenge with cancellous bone grafting is developing scaffolds that will provide the required mechanical load of the cancellous region while encouraging bone regeneration [27]. Traditional materials are strong yet often inflexible and incompatible with proper integration of host bone. Conversely, scaffolds such as PLA might be biocompatible but usually result in inadequate mechanical strength if designed at high porosity, a feature considered necessary for facilitating the ingrowth of tissues. This mechanical performance-biological functionality trade-off represents one of the most critical challenges when designing and optimizing 3D-printed scaffolds for cancellous applications [28].

Thus, the current study proposed undertaking the structural and parametric optimization of 3D-printed ST-PLA porous lattice structures for cancellous bone grafting applications to fill the existing research gap. This study contributes by optimizing key 3D printing parameters for ST-PLA scaffolds and integrating a response surface methodology to achieve targeted mechanical and surface properties, addressing gaps in scaffold design for cancellous applications. This work has incorporated the scaffold design's mechanical and surface roughness into a single study

Table 1
Summary of literature comparison of other research with our study.

Reference	Material studied	Compressive strength (MPa)	Key findings
Cox et al. [20]	PLA with controlled porosity	0.88	Demonstrated that controlled porosity significantly affects compressive strength.
Hassanajili et al. [21]	PLA-based scaffolds with composites	Suitable for low-load-bearing applications	Emphasized the role of material composition in achieving desired mechanical properties.
Dussault et al. [22]	PLA scaffolds for bone defect repair	Tailored to specific requirements	Highlighted the importance of structural optimization to balance mechanical performance and biological functionality.
Elhattab et al. [24]	PLA lattice structures	0.5–2.0	Low compressive strength was reported in simple cubic lattice designs.
Zhang et al. [25]	PLA	1.0–2.0	Observed low compressive strength in PLA scaffolds tailored for specific applications.
Rosso & Iannucci [26]	PLA	1.2–3.0	Analyzed compressive response of PLA, noting structural influence on strength.
Current study	ST-PLA with optimized porous lattice design	0.253–1.40	Achieved competitive compressive strengths without the use of composite materials. Employed a systematic optimization approach using Box-Behnken Design (BBD) for cancellous bone grafting applications.

through a systematic optimization process using an algorithm. The capability to proceed with in-depth research on how layer thickness, print speed, and cellular wall thickness changes would impact the mechanical and microstructural properties of the ST-PLA scaffolds. The results of this study significantly add value to the development of better bone graft materials for improved surgical outcomes and patient recovery in cancellous reconstruction. This study explores the optimization of 3D printing parameters for ST-PLA, focusing on enhancing compressive strength and surface roughness for cancellous bone implant applications. The paper is structured as follows: materials and methods are presented, detailing material selection and experimental procedures; results and discussion highlight statistical analysis, parameter effects on responses, and Scanning Electron Microscopy (SEM) analysis; experimental validation demonstrates the effectiveness of Multi-Input Multi-Output (MIMO) modeling for optimization; and conclusions provide a summary of findings and outline future research directions.

2. Experiments: materials and methods

2.1. Materials

The material used in this study was ST-PLA, bought from Creality company in China, which is a bio-based, ST-PLA filament derived from renewable corn starch feedstock and modified with proprietary additives to enhance its mechanical toughness and ductility. This modification improves material compatibility, thermal stability, and processing ease compared to standard PLA, making it ideal for applications requiring durability and resilience [29]. The choice of ST-PLA was deliberate, as its carbohydrate-based modification aligns with the objectives of this study, which is to evaluate high-performance, sustainable materials with improved mechanical properties. Moreover, it allows for higher quality and versatility in products while maintaining PLA's environmental benefits [30,31]. Detailed information on the utilized ST-PLA filament is given in Table (in supplementary material).

2.2. Response surface methodology

This study systematically investigated and optimized the relationships between the critical process parameters and mechanical properties of the 3D-printed ST-PLA samples using RSM. RSM is a powerful statistical method comprising mathematical and statistical tools that enable modeling and analyzing problems where several independent variables influence a dependent variable or response [32,33]. RSM is a powerful mathematical tool used to evaluate the relationships between multiple process parameters and one or more outcome variables. It has proven effective in material optimization, particularly in applications requiring trade-offs between mechanical strength, surface quality, and thermal behavior [34,35]. Therefore, the main aim of RSM in this work was to identify the best settings of layer thickness, print speed, and cellular wall thickness to maximize the mechanical performance of the printed parts and improve the surface roughness [36].

The experimental design consisted of a BBD, one of the most efficient RSMs for the response surfaces. The BBD was chosen over the Central Composite Design (CCD) for its efficiency in reducing the number of experimental runs while maintaining a robust framework for modeling. BBD explores the experimental domain uniformly, providing reliable results with fewer trials. Unlike CCD, which includes factorial, axial, and centre points, BBD avoids extreme factor levels, minimizing the risk of experimental failure or compromised 3D printing quality. Its ability to handle non-linear interactions between variables without extensive modifications to the experimental setup further supports its suitability for this study [37]. These input parameters are shown in Table S2 (in supplementary material). This experimental design gave a total of 17 runs with the addition of 5 center points to ensure the precision and replicability of the results. The center points also provided an estimate of the inherent variability in the process and, thus, a basis for checking the model's lack of fit and the presence of any curvature in the response surface. The approach helped find conditions for optimal printing. It provided an understanding of complex interactions between printing parameters, which is essential for developing more advanced and effective 3D printing processes with ST-PLA.

Fig. 1(a-d) has demonstrated the overview of testing methods. Fig. 1 (a) displays samples printed from ST-PLA. The authors produced three samples for each test, measured three Ra values, and averaged the results. The selection of parameters in this study, namely layer thickness, print Speed, and cellular wall thickness, is based on their significant impact on ST-PLA performance in FFF 3D printing. These parameters were specifically chosen due to their direct influence on printed parts' mechanical properties, structural integrity, and surface quality [38].

The authors chose between 45 mm/s and 80 mm/s for print speed. That was a well-calculated move to balance print quality with efficiency. A print speed below 45 mm/s is unnecessary; long print times are impracticable. On the other hand, speeds over 80 mm/s can lower the layer adhesion since there will not be enough time to cool down between layers. Three levels were considered for layer thickness: 0.1, 0.2, and 0.3 mm. Thus, it is possible to analyze the compromise between printing resolution by considering smaller layer thickness and the mechanical performance of parts. This range is standard for ST-PLA. It will provide insight into how layer thickness influences the printed samples' mechanical strength and surface finish.

Cellular wall thicknesses were tested at 0.4 mm, 0.7 mm, and 1.0 mm. Initial attempts to print cellular wall thicknesses below 0.4 mm were unsuccessful because prints could not be completed with sufficient structural integrity. Cellular wall thicknesses greater than 1.0 mm are well documented in the literature; however, resultant structures created using such a thickness tend to possess less overall porosity than desired for this study. The chosen range thus presents an optimum for investigating the balance of porosity-structural strength, which is of primary importance for applications where lightweight and simultaneously strong components are used. In the present study, these three input parameters are systematically investigated for their influence on the mechanical properties of ST-PLA using the BBD approach. Through a BBD method, the response surfaces can be effectively explored by conducting a manageable number of experimental runs. Seventeen experimental runs were conducted to ensure that the interactions between parameters were thoroughly analyzed without requiring an exhaustive number of tests.

By focusing on these specific ranges and incorporating the BBD approach, the methodology herein provides a holistic framework for optimizing conditions using 3D printing with ST-PLA, further extending the advances in high-performance applications of the material.

2.3. Measurement procedure

It can be observed from Fig. 1(b) that the compression test of the 3D printed ST-PLA samples, with their 36-mm by 36-mm dimensions, was carried out in this work by using the GTM 2500 Instrument. Tests were carried out at a cross-head speed of 1.3 mm/min, which was chosen by the requirement to make accurate and comparable measures of compressive strength for the different samples. Each specimen was compressed to failure, which allowed for an exact determination of the material's compressive strength and deformation characteristics for strains up to as high as 60 %. The tests were performed at a controlled temperature of 25 °C to simulate standard conditions and ensure consistency throughout different experiments. These results give the ability to value the ST-PLA material's structural integrity and load-bearing capabilities under changed printing conditions, thus providing essential treads for a complete understanding of its mechanical properties illustrated through the [39].

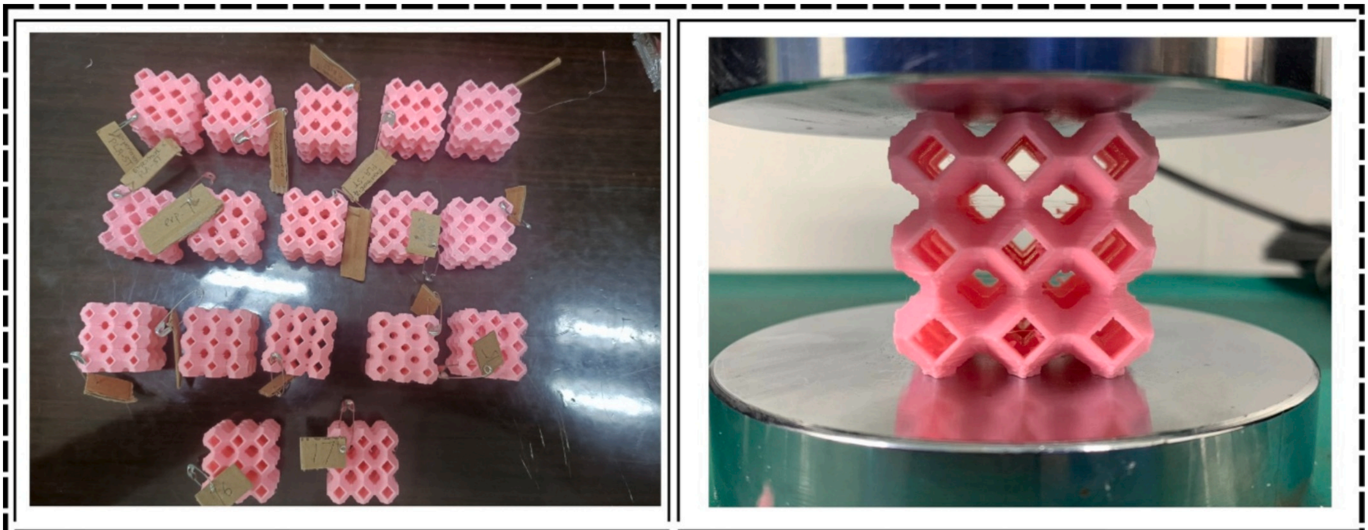

a) Modified novel Primitive structures

b) Compression analysis

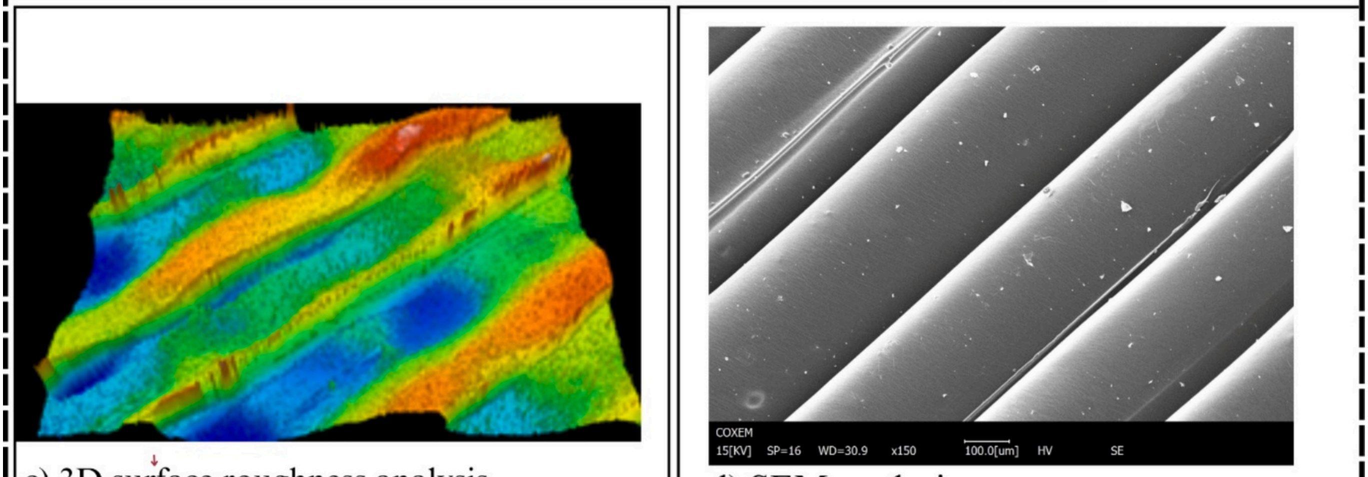

c) 3D surface roughness analysis

d) SEM analysis

Fig. 1. Overview of testing methods: (a) Modified novel primitive structures, (b) Compression testing setup for evaluating mechanical properties, (c) 3D surface roughness testing for assessing surface topography, and (d) SEM analysis for detailed examination of microstructural features and surface roughness distribution.

2.4. Surface roughness and SEM analysis

3D surface topography analysis was utilized for each printed sample to measure the arithmetic mean of surface roughness (Sa) and root mean square of surface roughness (Sq), with the help of Sensofar optical profilometer shown below in Fig. 1c. In this 3D surface profiling, three different measurement points within each lattice structure were measured to find the average value of Sa and Sq for a better understanding of the characteristics of the surface. The COXEM SEM testing machine was used to investigate the porosity and crack propagation, and microstructure analysis was also presented, as shown in Fig. 1d below. The specimens were cleaned using an air blower, and the sputtering coating was applied. The magnification of the carried-out SEM analyses was done at 70×, 150×, and 200×.

2.5. Analysis of TPMS structures in 3D printing: mathematical expression and impact of boundary conditions

The current Triply Periodic Minimal Surfaces (TPMS), exemplified by the Primitive (P-type) model, are studied for their application in 3D printing, guided by the mathematical expression shown in Fig. 2. This equation defines their structure and ensures minimal surface area and periodicity in three dimensions, making them ideal for optimizing material use and structural integrity in manufactured objects.

This work imposes different boundary conditions on properties and performance in TPMS. The original structure, whose boundary conditions are set at (0, 0, 0), retains a configuration with heightened sharpness and rigidity. It is fit for applications involving resistance to fracture and hence requires a significant amount of structural integrity. This will serve as the benchmark upon which changes in boundary conditions and their influence on the TPMS structures are compared.

In the modified pink model, the boundary conditions are changed from 0.9, 0.3, and 0.3, respectively, which causes a significant difference in the geometrical structure and physical properties of this structure. Due to this setting, all features are rounder and smoother; this means more capability for flexibility and distribution of stresses within the model. Such changes presuppose enhanced resistance to dynamic loads and a reduced probability of failure during mechanical stress, which enhances the implementability of the pink model in cases where high strength is combined with good adaptability.

Comparing the two models puts into perspective how essential boundary conditions are to TPMS. The white model is perfect for static applications, with its sharp, rigid features, while the enhanced flexibility and improved handling of stresses in the pink model open up

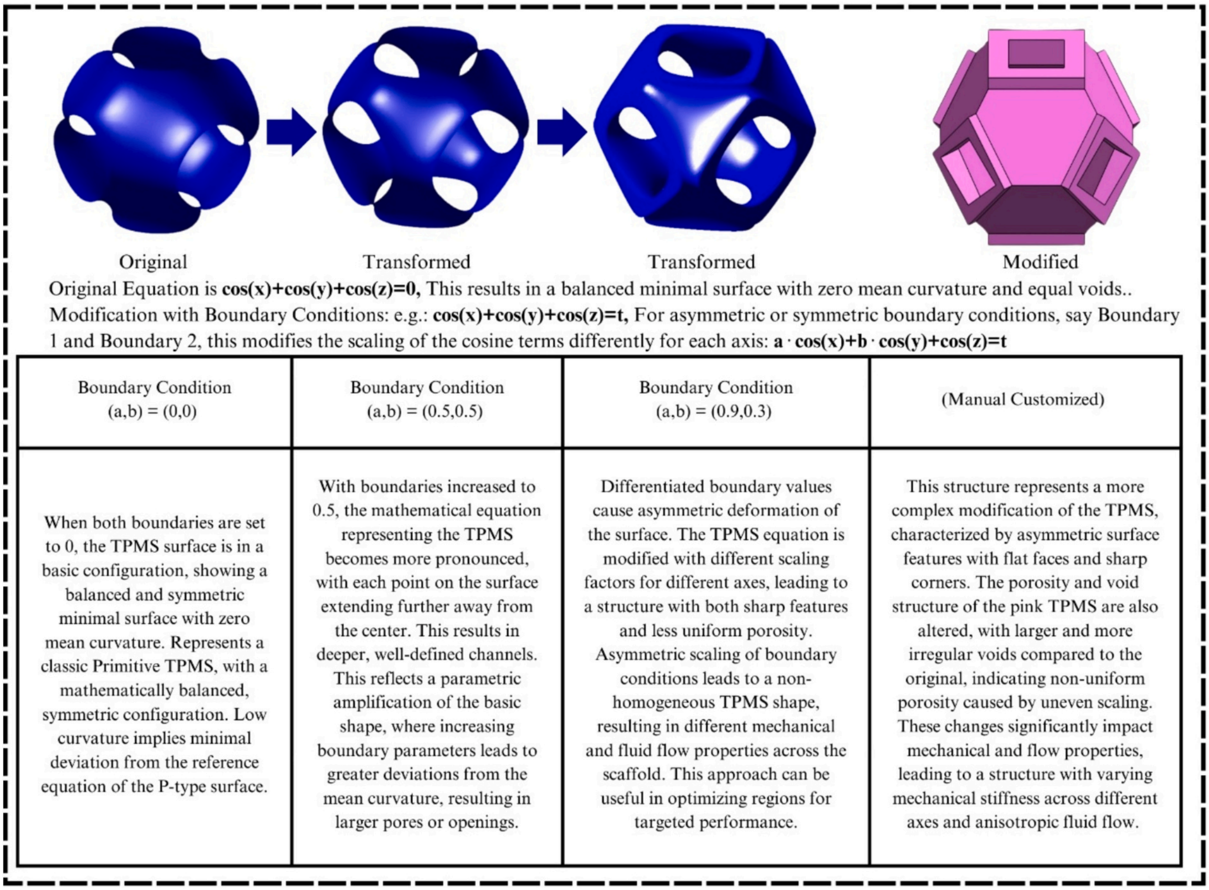

Original Equation is **cos(x)+cos(y)+cos(z)=0,** This results in a balanced minimal surface with zero mean curvature and equal voids..

Modification with Boundary Conditions: e.g.: **cos(x)+cos(y)+cos(z)=t,** For asymmetric or symmetric boundary conditions, say Boundary 1 and Boundary 2, this modifies the scaling of the cosine terms differently for each axis: **$a \cdot \cos(x)+b \cdot \cos(y)+\cos(z)=t$**

Boundary Condition (a,b) = (0,0)	Boundary Condition (a,b) = (0.5,0.5)	Boundary Condition (a,b) = (0.9,0.3)	(Manual Customized)
When both boundaries are set to 0, the TPMS surface is in a basic configuration, showing a balanced and symmetric minimal surface with zero mean curvature. Represents a classic Primitive TPMS, with a mathematically balanced, symmetric configuration. Low curvature implies minimal deviation from the reference equation of the P-type surface.	With boundaries increased to 0.5, the mathematical equation representing the TPMS becomes more pronounced, with each point on the surface extending further away from the center. This results in deeper, well-defined channels. This reflects a parametric amplification of the basic shape, where increasing boundary parameters leads to greater deviations from the mean curvature, resulting in larger pores or openings.	Differentiated boundary values cause asymmetric deformation of the surface. The TPMS equation is modified with different scaling factors for different axes, leading to a structure with both sharp features and less uniform porosity. Asymmetric scaling of boundary conditions leads to a non-homogeneous TPMS shape, resulting in different mechanical and fluid flow properties across the scaffold. This approach can be useful in optimizing regions for targeted performance.	This structure represents a more complex modification of the TPMS, characterized by asymmetric surface features with flat faces and sharp corners. The porosity and void structure of the pink TPMS are also altered, with larger and more irregular voids compared to the original, indicating non-uniform porosity caused by uneven scaling. These changes significantly impact mechanical and flow properties, leading to a structure with varying mechanical stiffness across different axes and anisotropic fluid flow.

Fig. 2. Reason and mechanism of selection of modified primitive structure.

possibilities of using TPMS within more dynamic environments. This constitutes a possible direction of research that this kind of TPMS could take in adaptive manufacturing scenarios, whereby it can tailor material properties toward specific functional requirements.

This pays for peering at mathematical control through the design and customization of TPMS for 3D printing. By changing the values along the boundary, the engineers and designers are thus able to have a significant influence on the mechanical properties of the print, enabling them to optimize structures across a wide range of applications. Being able to fine-tune properties by mathematical parameters indicates that theoretical mathematics has met practical engineering, and there is an expansive possibility for innovations in AM well into the future.

3. Results and discussion

3.1. *Statistical analysis using analysis of variance (ANOVA)*

3.1.1. *ANOVA for surface roughness*

Statistical analysis is crucial for identifying significant factors and their interactions in experimental studies, ensuring data-driven insights and the reliability of results. It validates models, optimizes processes, and provides a foundation for informed decision-making. The surface roughness parameters Sa and Sq were analyzed using ANOVA via Design Expert 13.0.5 software. The quadratic model for both responses was found statistically significant, with an F-value of 7.27 (p-value = 0.0031) for Sa and 7.45 (p-value = 0.0028) for Sq. Significant model terms were identified based on p-values less than 0.05. For Sa, the terms A (Layer Thickness), AB (Interaction between Layer Thickness and Print Speed), and A^2 (Quadratic term of Layer Thickness) were significant. Similarly, for Sq, the terms AB and A^2 were substantial. Table S3 and Table S4 (in supplementary materials) summarized the ANOVA results for Sa and Sq, respectively.

3.1.2. *Mathematical model for Sa*

The quadratic regression models derived from RSM provide a comprehensive understanding of the influence of 3D printing parameters on surface roughness (Sa and Sq). These models, expressed in coded and actual factors, help establish relationships between layer thickness, print speed, and the corresponding responses. The regression equations for Sa and Sq are presented below, representing the effect of individual parameters and their interactions on surface quality.

The interaction effects between layer thickness, print speed, and the resulting surface roughness metrics (Sa and Sq) are visualized using 3D surface plots. These plots illustrate the influence of each factor and their combinations on the response values.

The regression equations in coded factors for predicting Sa and Sq are as follows:

$$\mathrm{Sa} = 15.67 + 1.69\mathrm{A} - 0.0143\mathrm{B} - 2.59\mathrm{AB} - 4.97A^2 + 1.78B^2 \tag{1}$$

$$\mathrm{Sq} = 21.16 + 1.91\mathrm{A} - 0.3357\mathrm{B} - 3.59\mathrm{AB} - 7.56A^2 + 2.13B^2 \tag{2}$$

Fig. 3a and b illustrates the 3D surface plots for Sa and Sq, showing how the interaction between layer thickness and print speed affects surface roughness. These visualizations help identify optimal parameter ranges for achieving the desired surface finish.

Residuals' analysis further substantiates the validity of the model. Fig. 4(a) displays that the residuals for Sa are typically distributed, as shown by a normality distribution plot. A smaller residual value indicates the model's predictions are acceptably accurate. Fig. 4(b) showcases the correlation between predicted and actual values for Sa. In contrast, Fig. 4(c) evaluates the residuals against their expected values, demonstrating the adequacy and validity of the regression model.

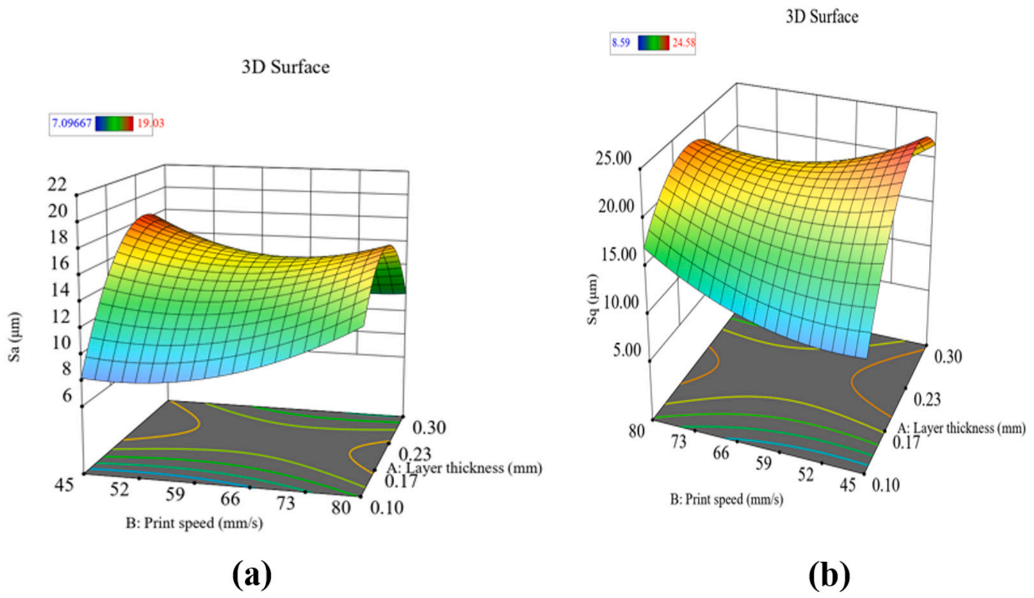

Fig. 3. 3D interaction plot for, (a) Sa and (b) Sq.

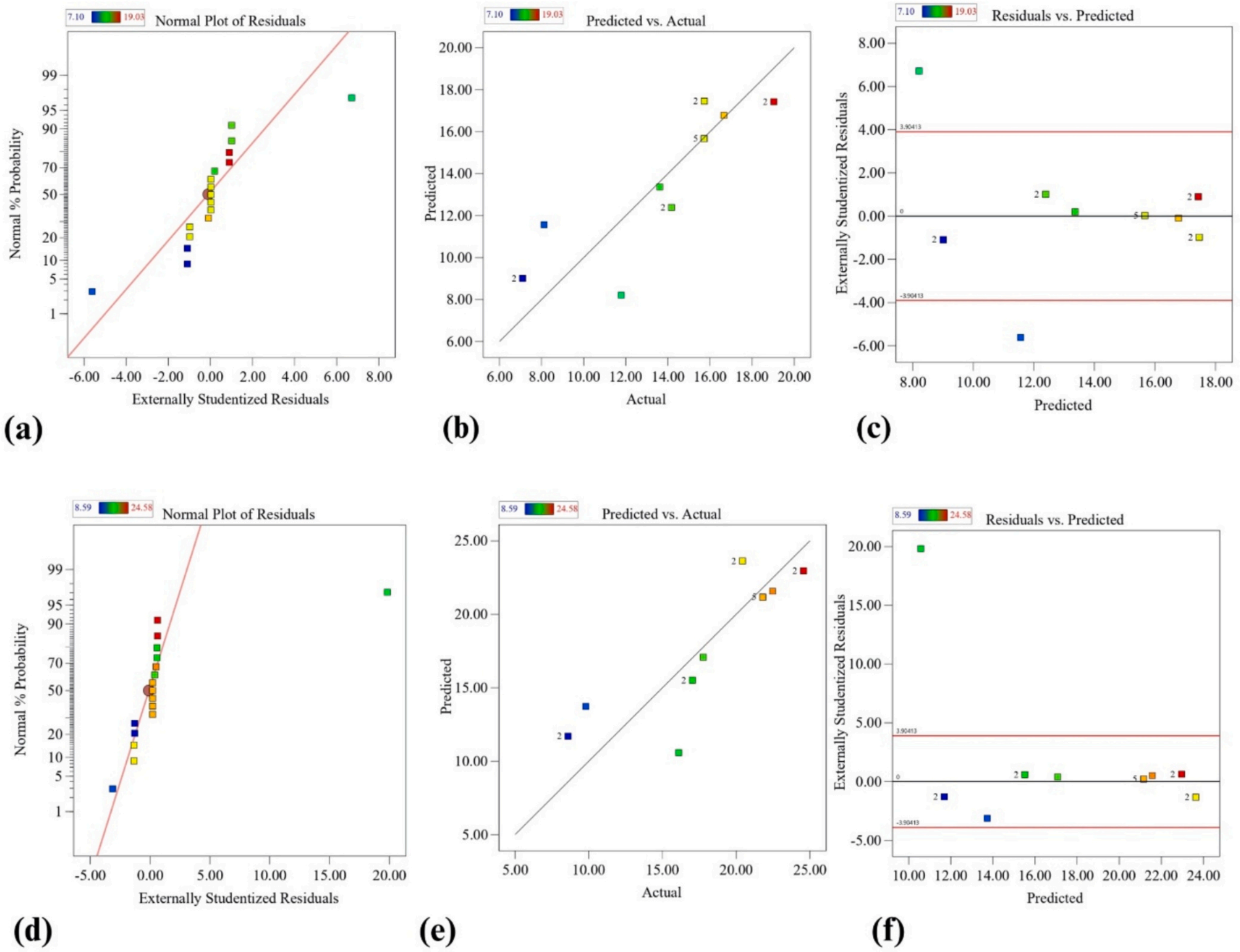

Fig. 4. Residual plots of Sa and Sq: (a) a percentile-based probability plot for Sa, (b) a graph depicting the relationship between predicted and actual values for Sa, (c) a chart displaying residuals vs. predicted values for Sa, (d) a probability plot centered on percentiles for Sq, (e) a graph contrasting actual vs. predicted values for Sq, and (f) a plot outlining residuals vs. predicted values for Sq.

Similarly, for Sq, Fig. 4(d) confirms the normality of residuals, Fig. 4(e) illustrates the relationship between actual and predicted values, and Fig. 4(f) evaluates residuals against their predicted values, ensuring the model's reliability and accuracy.

3.1.3. *ANOVA for compression testing*

Table S5 (in supplementary material) outlines the ANOVA results for compression testing. While the model is robust, a significant lack of fit (p-value = 0.0003) was observed, indicating potential limitations or data inconsistencies. Compression testing results were analyzed using the ANOVA technique via Design Expert 13.0.5 software. The analysis showed a significant quadratic model with an F-value of 18.29 and a p-value of 0.0005, indicating the model's statistical relevance. Among the studied factors, C (Cellular Wall Thickness), AC (Interaction between Layer Thickness and Cellular Wall Thickness), and C^2 (Quadratic term of Cellular Wall Thickness) were identified as significant, with p-values below 0.05. Other terms, including A (Layer Thickness) and B (Print Speed), were not statistically significant.

3.1.4. *Mathematical model for compression testing*

For set levels of every variable, utilizing actual variable expressions aids in making precise projections. It's pivotal to specify levels in original units for each factor. The linear regression models derived from RSM show the relationship in code with the input parameters. The Regression equation for compression testing is as follows;

$$\begin{aligned}\text{Compression Strength} = {} & 1.06 + 0.0589\text{A} + 0.0423\text{B} + 0.4176\text{C} \\ & + 0.0055\text{AB} + 0.1413\text{AC} + 0.0450\text{BC} \\ & - 0.0668\ \text{A}^2 + 0.0664\ \text{B}^2 - 0.3388\text{C}\end{aligned} \tag{3}$$

Fig. 5 validates the compression testing model. Fig. 5(a) confirms the normality of residuals, Fig. 5(b) shows strong agreement between predicted and actual values, and Fig. 5(c) demonstrates no evident patterns in residuals, ensuring model reliability.

The interaction effects between print speed and layer thickness on compression testing are visualized using 3d surface plots, as shown in Fig. S1 (in supplementary material). The primary and secondary horizontal axes represent the input variables, with the vertical axis showing the resultant TS and FS.

3.2. *Parametric effect on mechanical properties*

Several studies have shown that major 3D printing parameters such as layer thickness, infill density, and print speed affect the mechanical properties of printed parts, as shown in Figs. 6 and 7. For example, Cox et al. [20] demonstrated a compressive strength as low as 0.88 MPa in PLA scaffolds of controlled porosity, depending on structural design and porosity levels. Similarly, Hassanajili [21] et al. emphasized the material composition and structure that can be achieved to obtain mechanical properties suitable for applications that deal with low-load bearing. These results indicate a crucial relationship between process parameters and the final mechanical performance of materials 3D-printed.

The cell wall thickness proved to be the most relevant factor in compressive strength for this work, as explained by Dussault et al. [22], since increasing thickness leads to improved mechanical properties because of higher structural rigidity, as shown in Fig. 7a. Another relevant parameter for optimum mechanical performance is the interaction between layer thickness and cell wall thickness Fig. 7b shows an increase in the cellular wall thickness significantly enhances the compressive strength, whereas print speed has a relatively limited influence. The maximum load and compressive strength recorded from each standard run are plotted in Fig. 6. Among them, Standard Run 12, having a compressive strength of 1.405 MPa, showed the highest compressive strength since the layer thickness is in the middle and cellular wall thickness is high. On the contrary, Standard Run 9 possessed the lowest compressive strength of 0.253 MPa, probably due to its low cell wall thickness and printing speed. This agrees with findings by Cox et al. [20] since wall thickness and, subsequently, porosity play a decisive role in the integrity of structures and the mechanical performance of printed parts [40].

Chang et al. [41] have identified cellular wall thickness optimization in 3D-printed scaffolds or parts as essential in achieving a better load-carrying capacity. Cellular wall thickness, in the present study shown in Fig. 7c, was the dominant parameter and highly influenced mechanical strength, whereas the contribution of print speed was minimal. These findings illustrate that wall thickness has to be cautiously optimized for applications that demand high compressive strength, like bone grafting [42].

Fig. 7(d) shows the contour graph of compressive strength as a function of cellular wall thickness and print speed. This plot indicates that the scaffolds' compressive strength increases with cellular wall thickness but is independent of print speed. As the cellular wall thickness increases toward 1.0 mm, the compressive strength increases to a maximum, whereas strength is almost unaffected over the print speed range between 45 and 80 mm/s. Fig. 7(e) represents the dependence on cellular wall thickness and layer thickness. It is observed that an increase

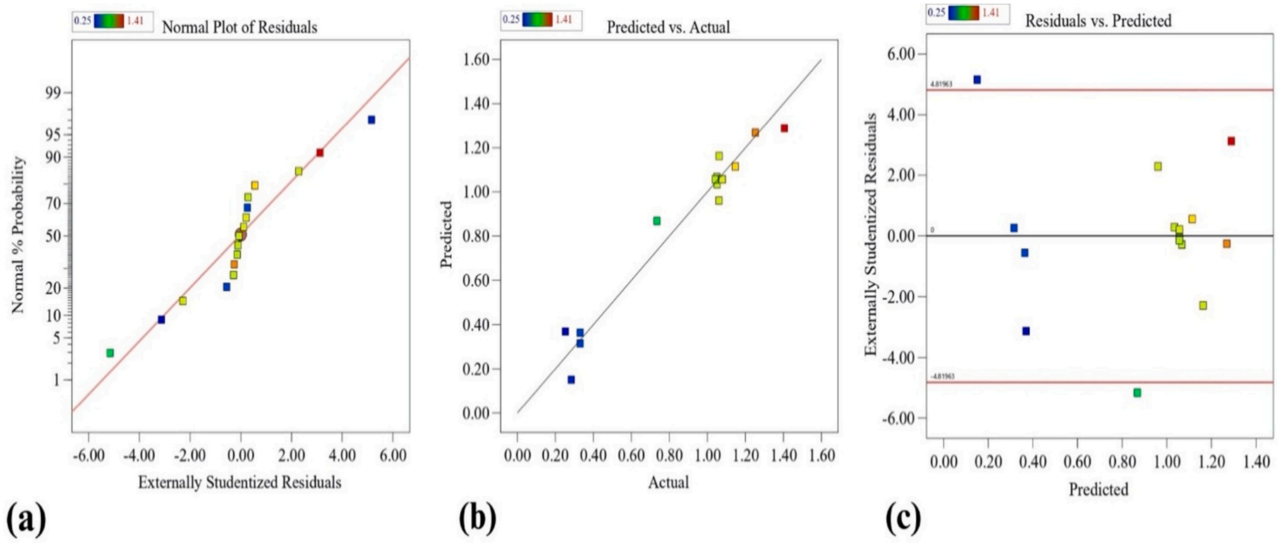

Fig. 5. Residuals analysis for compression testing: (a) normal plot of residuals, (b) predicted vs. actual values, and (c) residuals vs. predicted values.

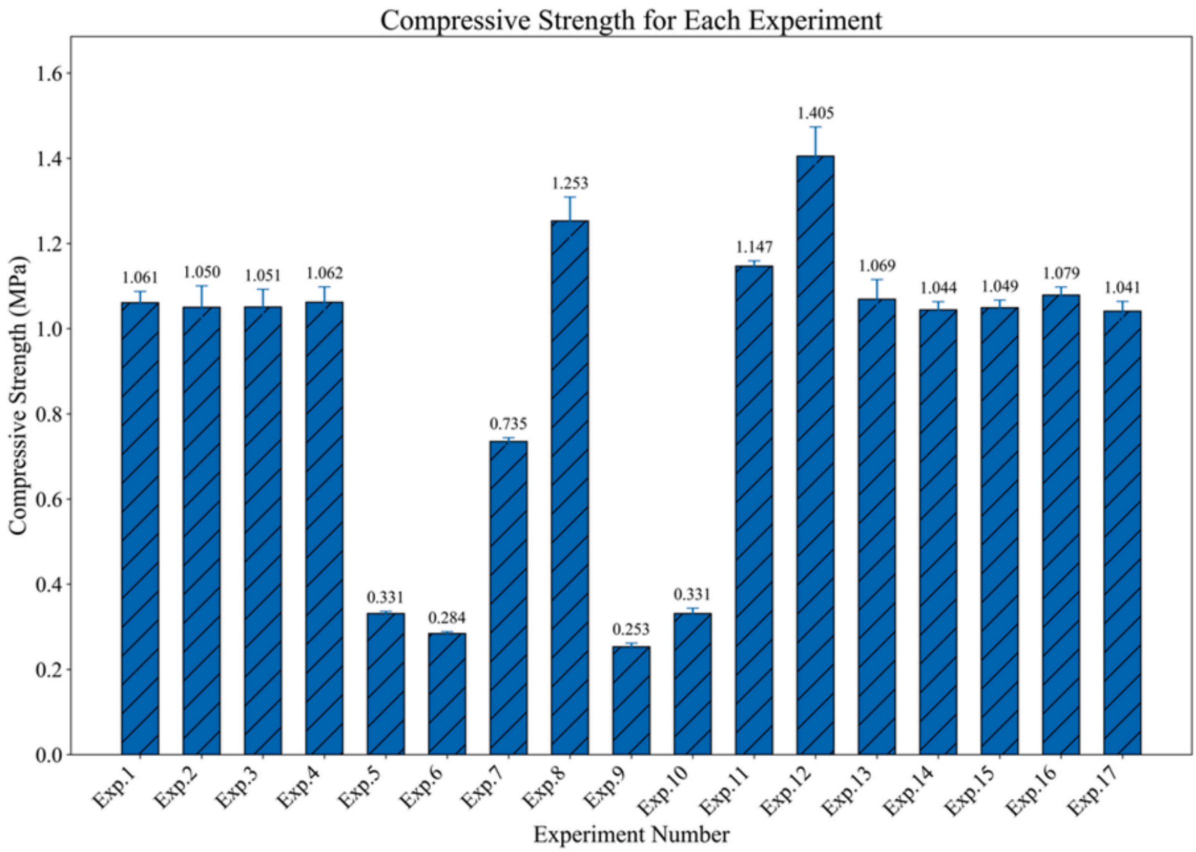

Fig. 6. Graphical representation of compressive strength by a standard run.

in layer thickness causes a limited increase in strength. With a maximum value of cellular wall and layer thickness, a maximum compressive strength of 1.4 MPa is attained.

Fig. 7(f) Contour plot of the interaction between layer thickness and print speed on the response of compressive strength: From this figure, the main effect of layer thickness is more significant to compressive strength than the speed of printing. It can be seen from the plot that with the increase in the layer thickness, the compressive strength increases, whereas the change in print speed insignificantly affects it.

Fig. 8 presents the SEM analyses, which further confirm that cellular wall thickness determines the mechanical properties of ST-PLA lattice structures. In Exp 8, its cellular wall thickness was 1.0 mm, contributing to the relatively high compressive strength of 1.253 MPa. From the SEM image shown in Fig. 8(a), a compact and homogeneous cellular structure exists with only several tiny defects, such as cracks or voids. This may be due to thicker walls, allowing for better dispersion of compressive forces within the material's internal structure. In addition, lattice structures with thicker walls have been said by [43,44] to increase compressive strength by improving load-bearing capabilities and reducing problems associated with localized stress concentrations leading to material failure. The experiment using a thickness of 1.0 mm exhibited the highest compressive strengths obtained from the study at 1.253 MPa. The SEM image, Fig. 8(a), which corresponds to this experiment, showed a dense and consistent cellular structure with few defects. Thicker walls will distribute the load better and reduce the risk of stress concentration and structure failure. This agrees with the established principles in material science: the denser the wall, the higher the mechanical stability due to better material resistance against compressive forces without deformation.

In contrast, the cellular wall thickness in Experiment 9 was 0.4 mm; hence, it showed a very low compressive strength of 0.253 MPa. Microcracks and voids presumably accounted for this in the corresponding SEM. Fig. 8(b), which demonstrates why the thin walls were more susceptible/suited to stress concentration/structural weaknesses. Since the thinner walls contain less material volume, the structure could not support the compressive load, resulting in premature failure. These findings agree with the general understanding that thinner-walled structures are more prone to mechanical failure when under load, owing to their lower capability to distribute stress effectively [45].

3.2.1. *Simulation and experimental comparison*

A comparison between the simulated and accurate responses of ST-PLA subjected to strain provides insight into the model's predictive capability, as shown in Fig. 9. The results indicated congruences and disparities at different strains up to a maximum of 60 %. This comparison suggests that FEA is effective in establishing an approximation of the mechanical behavior of ST-PLA under stress, especially on how reliable the same material will be for applications needing high accuracy in performance prediction. The data includes experimental and simulated stress measurements recorded at discreet strain intervals, including points at 7.5 %, 20 %, 25 %, 34 %, 42 %, 48 %, and 60 %. Note that this FEA model represents idealized conditions and thus will always predict a slightly higher stress response than that obtained experimentally, especially at the lower strain values. For instance, at a strain of 7.5 %, experimental measurements have a stress of 1.37 MPa, while the simulated model achieves 1.69 MPa. This can be achieved through inherent assumptions regarding homogeneity and isotropy in the FEA model, most of the time for simplification, which does not account for possible microstructural irregularities in ST-PLA. These minor differences point to material properties, which can be minor anisotropy or microscopic imperfections that reduce stress more than in actual samples at lower strains.

In comparison, at higher strains, the model captures better alignment between experimental and simulated stress responses [46]. For 42 % and

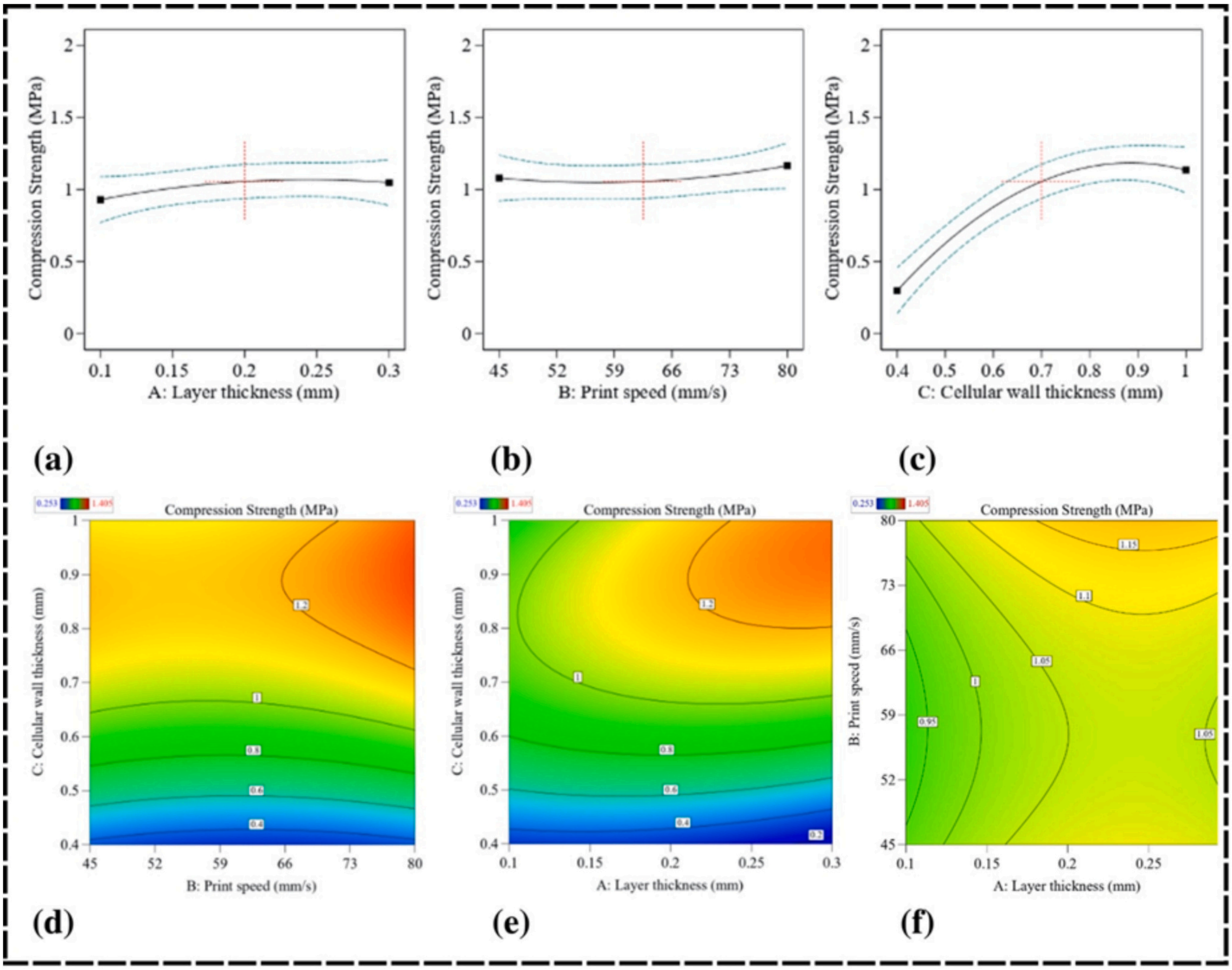

Fig. 7. The effect of process parameters on compressive strength for ST-PLA: (a) layer thickness, (b) print speed, (c) cellular wall thickness, (d) show the interaction between print speed and cellular wall thickness, (c-d) show the interaction between layer thickness and cellular wall thickness. (f) Show the interaction between layer thickness and print speed.

48 % strain values, experimental stresses are around 0.97 MPa and 0.83 MPa, while the simulated corresponding results remain constant at 1.20 MPa. This convergence conveys that the assumptions considered in the FEA model are that all elasticity and plasticity properties correspond well with actual material behavior in the case of moderate strain. With these intermediate strain levels, the material is likely to exhibit behavior in which the FEA model captures strain hardening or stiffness enhancement.

The highest strain levels analyzed include 60 % strain, which also shows a strong agreement between simulation and experiment, in which the experimental stress was recorded at 1.40 MPa and simulated stress was 1.73 MPa. This close correspondence at high strains proves that the material model's parameters are correct, especially those related to yield strength and ultimate tensile characteristics. This would imply that the FEA simulation is a good representative of the structural behavior of the material in the high-strain domain, where deformations become more linear and predictable.

Results of this comparison show good agreement for the FEA model throughout most of the strain levels, with further refinement possible at the lower level of strains. The deviation at the lower strain level can be improved by refining the material modeling methodology to capture the microstructural characteristics peculiar to stereolithographic polymers like ST-PLA. For example, the incorporation of anisotropic behavior or, even more so, viscoelastic effects could yield a simulation that is closer to the actual material behavior because these attributes are usually very significant in accurate polymeric materials [47]. In addition, even boundary conditions are idealized in simulations for easier calculation compared to an experiment where load-shared distribution or alignment of the sample may not be perfect. Such changes to the boundary conditions in the simulation environment could easily make the simulated displacements compare better at the beginning of the deformation process.

Although the FEA model has been reliable in capturing the mechanical response of the ST-PLA material, data obtained from this study indicated that refinement of some simulation parameters could be done to enhance prediction accuracy for most of the spectrum of strain. Fig. S2 (in supplementary material) reiterates that any simulation result should always be checked against experimental data where meaningful and accurate predictions are expected, but in particular, high material performance accuracy, for instance.

3.3. Parameteric effects on surface roughness

The surface roughness of 3D-printed samples was quantified by Sa, representing average surface roughness, and Sq, under the name root mean square surface roughness, both calculated from 3D surface roughness maps. This analysis demonstrated that layer thickness and print speed are the most relevant parameters affecting surface texture.

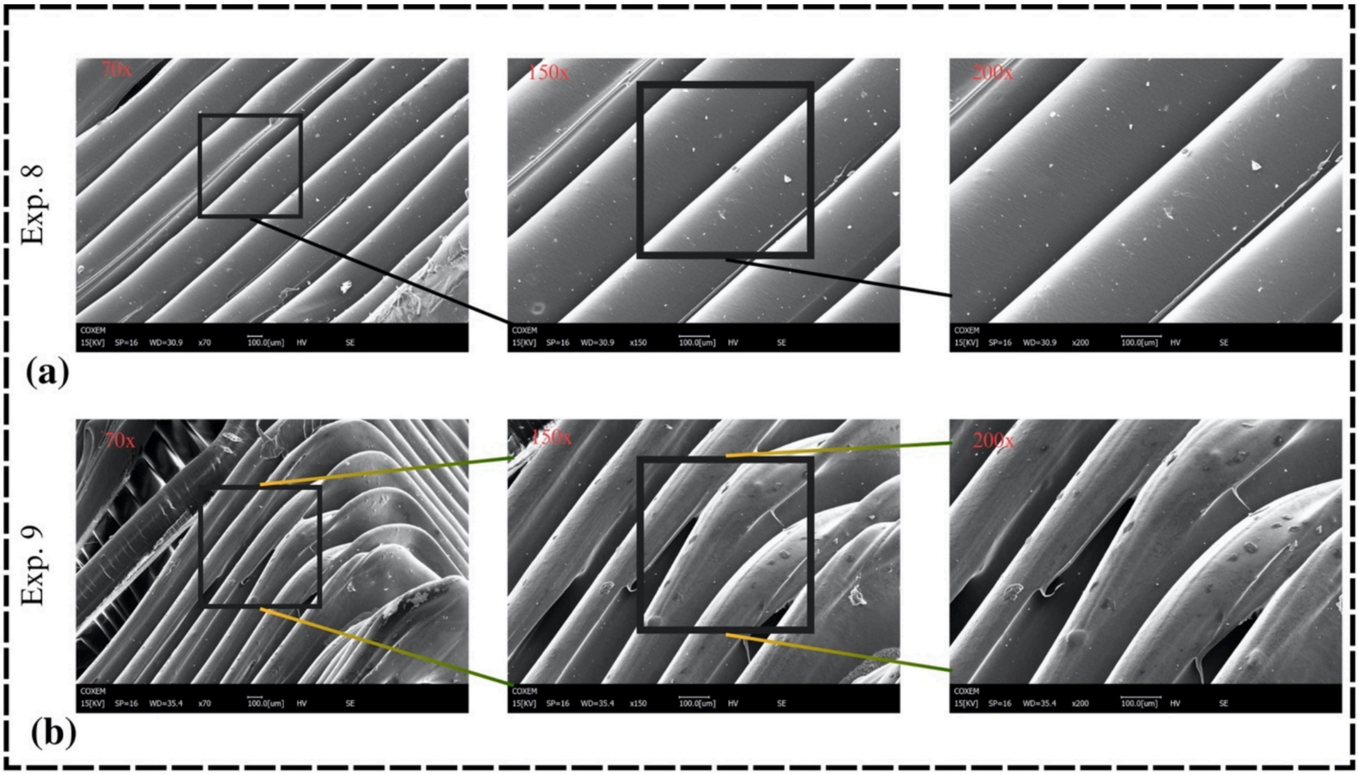

Fig. 8. SEM and representation of samples; a) Exp.8, b) Exp.9.

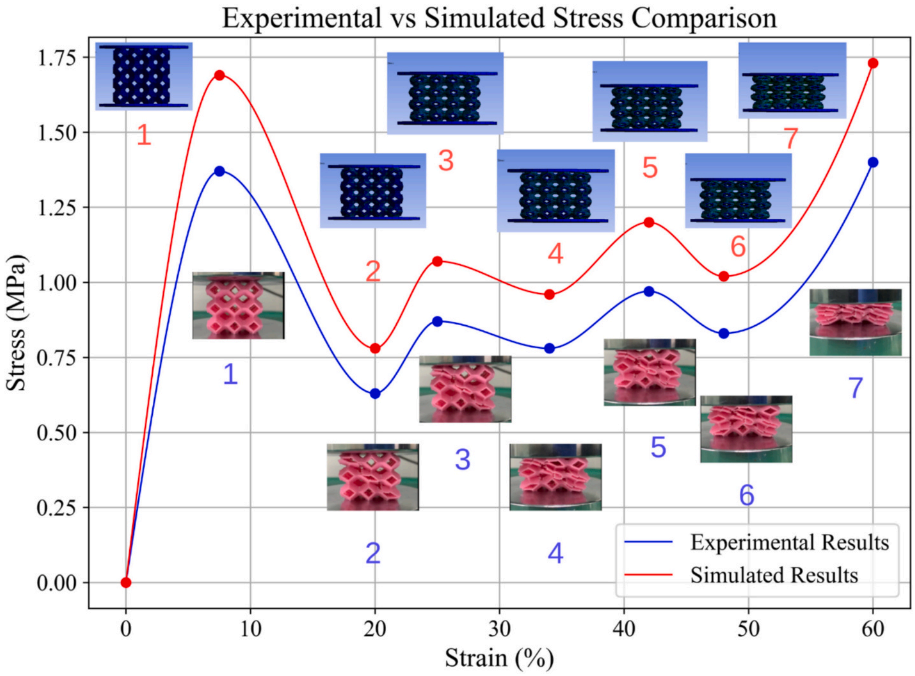

Fig. 9. Stress-strain curves comparing simulation and experimental results.

Thinner layers and low printing speed produced generally smoother surfaces, while increasing the layer thickness or printing speed tended to raise the surface roughness.

3.3.1. *Effect of layer thickness on surface roughness*

Layer thickness was one of the main determinants of surface roughness [48]. The thinner the layers applied, the smoother the surface they produced because a smaller height difference between successive layers produced fewer surface irregularities. Thicker layers developed into more exaggerated ridges between and valleys within layers, producing correspondingly rougher surfaces.

Fig. S3 (a-h) (in supplementary materials) has portrayed the 3D profilometry of different samples. Taking a layer of 0.1 mm with a print speed of 45 mm/s in Experiment 1, the surface roughness resulted in relatively low values: Sa = 11.78 µm and Sq = 16.1 µm. Thinner layers can provide better precision in material deposition, resulting in minimum ridge formation between the layers. The 3D roughness map clearly shows this is a much smoother surface, with a very flat profile and few peaks and valleys. For Example, 5, the layer thickness was maintained at 0.1 mm, while the print speed was varied at 62.5 mm/s; the surface roughness values came to be even lower: Sa = 7.09 µm and Sq = 8.59 µm. These observations are again visually realized from the SEM image of Experiment 5, which shows a smooth and uniform surface with only a few defects. A reduction in the height difference of successive layers due to the presence of thin layers decreases surface defects, developing a finer surface texture [49].

Meanwhile, with the increase in thickness, the surface roughness increased significantly. In Experiment 2, when layer thickness was increased to 0.3 mm, and the print speed was kept at 45 mm/s, the surface roughness values increased significantly to Sa = 16.16 µm and Sq = 22.47 µm. The 3D roughness map of Experiment 2 had more accentuated ridges and valleys than Experiment 1, showing that the thicker layers introduced more significant height discrepancies among adjacent layers. Further, this resulted in a higher roughness of the texture. The step effect increases when a larger volume of material is deposited per layer, which enhances these surface imperfections. This was continued in Experiment 6, with the layer thickness being 0.3 mm and a print speed of 62.5 mm/s. The values for the surface roughness were high, showing that Sa = 14.17 µm and Sq = 17.03 µm, confirming again that with thicker layers, increased surface roughness is achieved independent of print speed. The 3-D roughness map for Experiment 6 is shown to identify a similar pattern compared to Experiment 2 with pronounced surface defects of peaks and valleys.

3.3.2. *Effect of print speed on surface roughness*

Print speed also significantly influenced surface roughness, mainly due to its effect on the precision of material deposition. Slower print speeds had much better control over the deposition process, giving smoother surfaces. In contrast, with increasing speeds, the surfaces normally became more and more disturbed since the bonding between layers was imperfect, and more defects appeared on the surface [50,51].

In the case of Experiment 3, the layer thickness retained its former value of 0.1 mm, but the printing speed increased; the surface roughness values were higher than in Experiment 1, with Sa = 13.61 µm and Sq = 17.77 µm. With increased print speed, the accuracy of material placement is reduced; hence, the undulations on the surface are more evident from the 3D roughness map. With the faster speed, although the layer thickness was still thin, it introduced surface imperfections. Theoretically, thinner layers reduce surface roughness, but an increased print speed counters this effect by reducing the time the material cools between layers, which causes the material to bulge.

Also, Experiment 10, which deals with the layer thickness of 0.2 mm at a printing speed of 80 mm/s, gave the maximum surface roughness values for the entire study: Sa = 19.03 µm and Sq = 24.58 µm. A higher speed increased the height difference between layers, creating more irregularities on the surface that raised the surface roughness. The 3D roughness map for experiment 10 shows significant peaks and valleys, proving that combining thicker layers with faster print speed results in inferior surface quality. The faster deposition reduced the cooling time between layers, which caused less accurate bonding between layers and, hence, sharp ridges and valleys [52].

In cases of slower printing speed, the material deposited was better, offering finer surface quality. For example, Experiment 11, with a 0.2 mm layer thickness and printing speed of 45 mm/s, had lower surface roughness values than Experiment 10: Sa = 15.73 µm and Sq = 20.423 µm. SEM images as depicted in the Fig. S4(a-c) (in supplementary material) shows more pronounced ridges and undulations than thinner-layered experiments. The reduced print speed in this run somewhat controlled the deposition process and reduced roughness. Although thicker layers developed a rougher surface, as one might anticipate, slowing the speed mitigated the negative effect of layer thickness on surface roughness to some degree. This agrees with the literature in that most argue that with low speeds, material deposition becomes more controlled, resulting in a better surface finish, even though these layers can be thicker [53].

This corresponded to the following roughness values for Experiment 13, using a layer thickness of 0.2 mm and a print speed of 62.5 mm/s: Sa = 15.72 µm and Sq = 21.08 µm. The SEM image from Exp 13 c presents a surface with bulging and pronounced ridges, hence quite rough. The material deposition was somewhat controlled, given that this test had a moderate print speed. However, because this test has a higher layer thickness compared with other tests and a relevantly higher print speed, surface irregularities are greater than those acquired in tests with thinner layers. The 3D roughness map of Exp 13 affirms these observations visually. From this, one can see that there exist remarkable ridges and valleys on the surface, which means there is a higher surface roughness [54].

Surface roughness analyses across the experiments evidence that, among others, the layer thickness and print speed were the most determining factors regarding the final surface quality of 3D-printed parts. Thin layers, as in Experiments 1 and 5, always produced smoother surfaces with lower Sa and Sq values when combined with medium print speeds. Thicker layers, such as in Experiments 2, 6, and 10, resulted in rough surfaces with the step effect between layers, which became larger upon increasing print speed. SEM images for Experiments 5, 11, and 13 validate these observations by visually showing that the surface defects were less severe in thinner-layer experiments. At the same time, the ridges and bulging were more pronounced in thicker-layer experiments at higher speeds. These large format 3-D surface roughness maps provided a clear visualization of these trends and showed how layer thickness and print speed interact in influencing surface quality.

Layer thickness and print speed will need to be optimized for 3D-printed parts with smoother surfaces since the best results on surface finish are achieved with thinner layers at slower speeds. These findings are expected to support established research regarding parameter selection to control surface roughness by additive manufacturing.

4. Multi-input multi-output optimization method

In the context of the mechanical properties of lattice structures, the authors proposed a multi-input multi-output (MIMO) model to predict compressive strength and surface roughness. This model can aid in the parametric optimization of lattice structures and guide the design for improved cancellous bone graft applications.

4.1. *Mathematical model for predicting compressive strength and surface roughness*

To accurately predict the mechanical performance of 3D-printed scaffolds, it is essential to develop a mathematical model that can integrate multiple process parameters and output physical properties such as compressive strength and surface roughness. The MIMO model proposed here considers key parameters (layer thickness, print speed, and cellular wall thickness) to provide insight into the resultant mechanical properties, as shown in Fig. S5 (in supplementary material).

The formulation of the MIMO model is expressed as follows:

$$o_1 = \sum_{i=1}^{n} \sigma\left[h_i w_{(h_i o_1)}\right] \tag{1}$$

$$o_2 = \sum_{i=1}^{n} \sigma\left[h_i w_{(h_i o_2)}\right] \tag{2}$$

where, o_1 is the first output, h_i is the internal state, $w_{(h_i o_1)}$ is the weight parameter between the internal state h_i and output o_1 and n is the total number of hidden states. The *m*th output is defined as:

$$o_m = \sum_{i=1}^{n} \sigma\left[h_i w_{(h_i o_m)}\right] \tag{3}$$

where, $o_m \in \mathscr{R}$ is the output response, corresponding to different mechanical properties like compressive strength and surface roughness, h_i represents the hidden states within the model, which capture internal dynamics based on input variables. $w_{(h_i o_m)}$ denotes the weight connecting the hidden state.

This approach allows for the accurate prediction of multiple performance metrics based on the same input conditions, offering an integrated perspective on scaffold performance. The integration of multiple input variables ensures the model is highly adaptable for predicting a range of mechanical properties under various printing conditions. The hidden state h_1 is defined as:

$$h_1 = \sum_{j=1}^{l} \sigma\left[I_j w_{jh1}\right] \tag{4}$$

$$h_2 = \sum_{j=1}^{l} \sigma\left[I_j w_{jh2}\right] \tag{5}$$

where I_i is the *j*th input of the model such that $j = \{1, 2, .., l\}$, w_{jh1} is the weight of *j*th input for the state h_1. In general, the state h_n is defined as:

$$h_n = \sum_{j=1}^{l} \sigma\left[I_j w_{jhn}\right] \tag{6}$$

From Eqs. (5) and (6) we can get:

$$o_m = \sum_{i=1}^{n} \sigma\left[w_{(h_i o_m)} \sum_{j=1}^{l} \sigma[I_i w_{ihn}]\right] \tag{7}$$

where sigmoid function, (x), is defined as

$$\sigma(x) = \frac{1}{1 + e^{-x}} \tag{8}$$

The model defined in Eq. (7) is trained using the swarm optimization technique. The model parameter identification is achieved by following the minimization problem:

$$J = [O - \widehat{O}]^2 \tag{9}$$

where $\widehat{O}$ is the augmented output, and O is the output measured from the actual system, defined as,

$$O = \begin{bmatrix} o_1 \\ o_2 \\ \vdots \\ o_m \end{bmatrix} \tag{10}$$

The objective function is solved as a minimization problem to find the weight matrix $Q_h \in \mathscr{R}^{H \times I}$ and $Q_o \in \mathscr{R}^{M \times H}$:

$$Q_h = \begin{bmatrix} w_{1h1} & \cdots & w_{Ih1} \\ \vdots & \ddots & \vdots \\ w_{1hH} & \cdots & w_{IhH} \end{bmatrix} \tag{11}$$

$$Q_o = \begin{bmatrix} w_{(h_1 o_1)} & \cdots & w_{(h_H o_1)} \\ \vdots & \ddots & \vdots \\ w_{(h_1 o_M)} & \cdots & w_{(h_H o_M)} \end{bmatrix} \tag{12}$$

where H is the number of hidden states, I is the number of inputs of the mathematical model, and M is the number of outputs.

4.2. Applications of the Model to ST-PLA Lattice Structures

By applying this model to the dataset generated in our study, we can predict how different combinations of layer thickness, print speed, and cellular wall thickness will affect the mechanical performance of the ST-PLA lattice structures. The model provides a predictive tool for optimizing the 3D printing process, reducing the need for exhaustive trial-and-error experimentation, and enabling more precise control over scaffold properties. The effect of Layer thickness and print speed on compressive testing, Sa, and Sq are shown in Fig. S6 (in supplementary material).

The model confirmed that for surface roughness, minimum values of 6.98 μm for Sa and 8.38 μm for Sq were obtained when the layer thickness was set to 0.1 mm and the printing speed to 61 mm/s. This confirmed the general intuition that smaller layer thicknesses lead to smoother surfaces, as the thin layer thickness reduces the “stair-stepping” effect responsible for surface irregularities. Often, higher print speeds tend to increase surface roughness due to insufficient time for material settlement; however, combined with finer layer thickness, it worked oppositely to decrease roughness. The same concept was evident in literature reviews: Ursini [55] similarly noted that thinner layers improve surface smoothness, which is crucial for applications requiring high surface quality.

In contrast, the maximum values for Sa, 21.76 μm, and Sq, 24.68 μm, were obtained with a layer thickness of 0.28 mm and a print speed of 53 mm/s. The coarse surface generated by a larger layer size was due to increased step layering, which enhanced roughness. While lower print speeds allowed better layer fusion when combined with a larger layer thickness, a pronounced surface texture resulted.

The model predicted the minimum strength for compressive strength with a layer thickness of 0.3 mm, print speed of 59.5 mm/s, and cellular wall thickness of 0.4 mm. This was explained by thin walls not providing sufficient material to resist compressive forces, and the higher print speed contributed to weaker bonding between layers, further reducing strength. Ergene et al. [56] similarly found that structures with thinner walls generally exhibited lower compressive capabilities due to reduced material available to resist stress.

The highest compressive strength, 1.38 MPa, was obtained with the same layer thickness of 0.3 mm but with a lower print speed of 45 mm/s and a cellular wall thickness of 0.93 mm. In this case, the thicker cellular walls provided more significant cross-sectional areas, which effectively distributed compressive loads, thus improving strength. The slower printing speed allowed for better adhesion between layers, enhancing the structural integrity of the printed object. This finding is consistent with those of Netto [57] and Kumar [58], who demonstrated that, in similar lattice structures, increasing wall thickness enhances load-bearing capacity.

This model revealed transparent relationships between process parameters and the structural properties of specimens. Applications requiring smoother surfaces, therefore, utilized finer layers at moderate print speeds, while applications needing higher strength levels employed thicker cellular walls and optimized print speeds. By predicting these relationships, the model significantly reduced the need for trial-and-error testing, helping researchers achieve the desired structural properties efficiently.

The model’s flexibility allows it to optimize outputs by increasing or decreasing predicted values based on the application’s requirements as exhibited in the Table S6 (in supplementary material). The model can enhance surface roughness or mechanical properties by adjusting layer thickness, print speed, and wall thickness. For instance, if a smoother surface finish is required, the model can suggest parameter adjustments like a finer layer thickness, potentially lowering surface roughness values. Conversely, if greater compressive strength is needed, the model can recommend increasing wall thickness or adjusting print speed to achieve higher strength outputs. This adaptability makes the model valuable, as it can predict and suggest the best parameter combinations to meet diverse performance goals, reducing the need for extensive trial and error in 3D printing optimization [55]. The future of scaffold manufacturing increasingly hinges on 4D printing, with biocompatible polymers being tailored to react to dynamic physiological stimuli like temperature, pH, or stress. Such materials have smart shape-memory properties, allowing time-programmable transformations and stimuli-activated drug release. ST-PLA, a modified PLA-based material, is a promising candidate owing to its compatibility with programmable printing and responsiveness [59,60]. Incorporating this functionality in ST-PLA architecture will potentially make the material more adaptable in the in vivo environment, particularly when applied to anatomically dynamic load-bearing sites.

5. Conclusions and prospects

This work was performed to investigate the potential of bio-based super tough Polylactic Acid (ST-PLA), derived from renewable corn starch feedstock and modified with mechanical toughening agents, as a promising material for cancellous bone implants. By leveraging its enhanced mechanical strength and surface smoothness, ST-PLA showed excellent compatibility for biomedical applications requiring lightweight, porous structures that mimic natural bone properties. Through Box-Behnken Design (BBD) optimization and a Multi-Input Multi-Output (MIMO) predictive model, the study systematically investigated and optimized critical 3D printing parameters, including layer thickness, print speed, and cellular wall thickness. The specific conclusions made from this simulation and Experimental study include:

i. The use of bio-based ST-PLA, derived from renewable corn starch feedstock and modified with mechanical toughening agents significantly improved its mechanical properties, achieving around 28 % improvement in compressive strength (1.405 MPa) and approximately 25 % increase in elastic modulus (0.075 GPa) compared to previously published ST-PLA-based materials, making it highly suitable for cancellous bone implants.
ii. The optimized ST-PLA scaffolds exhibited surface roughness values of 6.98 μm (Sa) and 8.38 μm (Sq), ideal for promoting osseointegration and minimizing the risk of failure at the material-bone interface. SEM analysis confirmed reduced porosity and improved interlayer bonding, contributing to enhanced mechanical stability and biological compatibility.
iii. While the elastic modulus of the ST-PLA scaffolds is lower than that of human cancellous bone, it effectively reduces stress shielding, which is crucial for ensuring better long-term integration with surrounding tissues. This finding positions ST-PLA as a promising candidate for low-load-bearing bone grafts.
iv. The study highlighted the potential of ST-PLA as a customizable material for patient-specific implants. Its ability to be tailored through 3D printing techniques offers the possibility of achieving highly precise and optimized grafts that enhance surgical outcomes and promote faster patient recovery.
v. This work was limited to in vitro testing, and further, in vivo studies are necessary to validate the performance of ST-PLA under dynamic physiological conditions. Additionally, scalability for industrial production and the integration of bioactive molecules for enhanced tissue regeneration requires further investigation.
vi. Future work should focus on advancing bio-functionalization techniques to improve tissue integration and incorporating growth factors to enhance osteointegration. Expanding the application of ST-PLA to other biomedical fields, such as spinal and orthopaedic implants, is crucial for exploring its broader potential. Furthermore, bio-printing and 3D printing advancements could further optimize the scalability and manufacturing of ST-PLA scaffolds for clinical use.

CRediT authorship contribution statement

Ray Tahir Mushtaq: Writing – original draft, Conceptualization. **Ghulam Hassan Askari:** Writing – original draft, Conceptualization. **Chengwei Bao:** Writing – original draft, Conceptualization. **Yanen Wang:** Writing – original draft, Conceptualization. **Khubab Ahmed:** Writing – original draft, Conceptualization. **Aqib Mashood Khan:** Writing – original draft, Conceptualization. **Shubham Sharma:** Writing – review & editing. **Mohammed Alkahtani:** Writing – review & editing.

Consent to participate

Not applicable.

Consent to publish

All authors have read and approved this manuscript.

Ethical approval

Not applicable.

Funding

This work was supported by Researchers Supporting Project Number (RSP2025R274), King Saud University, Riyadh, Saudi Arabia.

Declaration of competing interest

The authors declare that they have no known competing financial interests or personal relationships that could have appeared to influence the work reported in this paper.

Acknowledgments

This work was supported by Researchers Supporting Project Number (RSP2025R274), King Saud University, Riyadh, Saudi Arabia. The work is also supported by “the Fundamental Research Funds for the Central Universities” (D5000240313), and The Research Fund for International Scientists (RFIS) of the National Natural Science Foundation of China GIA24002.

Appendix A. Supplementary data

Supplementary data to this article can be found online at https://doi.org/10.1016/j.ijbiomac.2025.144466.

Data availability

All the datasets used to support the findings are available within this manuscript.

References

[1] M. Rehman, Y. Wang, K. Ishfaq, R.T. Mushtaq, M. Alkahtani, A novel methodology for developing dense and porous implants on single generic optimized setting for excellent bio-mechanical characteristics, J. Mater. Res. Technol. 33 (2024) 2593–2611, https://doi.org/10.1016/j.jmrt.2024.09.209.
[2] M.V. Varma, B. Kandasubramanian, S.M. Ibrahim, 3D printed scaffolds for biomedical applications, Mater. Chem. Phys. 255 (2020) 123642, https://doi.org/10.1016/j.matchemphys.2020.123642.
[3] P.R. Kumar, Dipen Kumar, Muazu Abubakar, Syed Gazanfar Mustafa Ali, Manowar Hussain, 3D printing technology for biomedical practice: a review, J. Mater. Eng. Perform. 30 (2021) 5342–5355, https://doi.org/10.1007/s11665-021-05792-3.
[4] T. Han, S. Kundu, A. Nag, Y. Xu, 3D printed sensors for biomedical applications: a review, Sensors (Basel) 19 (7) (2019) 1706, https://doi.org/10.3390/s19071706.

[5] M.P. Silva, S. Isabel, José A. Covas, Natália M. Alves, Maria C. Paiva, 3D printing of graphene-based polymeric nanocomposites for biomedical applications, Funct. Compos. Mater. 2 (2021) 1–21, https://doi.org/10.1186/s42252-021-00020-6.

[6] C. Bao, Y. Wang, G. Pearce, R.T. Mushtaq, M. Liu, P. Zhao, M. Liu, R.T. Mushtaq, In-situ additive manufacturing with lunar regolith for lunar base construction: a review, Appl. Mater. Today 41 (102456) (2024) 102456, https://doi.org/10.1016/j.apmt.2024.102456.

[7] C. Bao, Y. Wang, G. Pearce, P. Zhao, M. Liu, R.T. Mushtaq, 3D printing of regolith-based epoxy composites with excellent temperature resistance and mechanical strength, Acta Astronaut. (2025).

[8] M. Mojaver, T. Azdast, R. Hasanzadeh, An experimental and numerical study on an innovative metastructure for 3D printed thermoplastic polyurethane with auxetic performance, Polym. Adv. Technol. 35 (2) (2024) e6298, https://doi.org/10.1002/pat.6298.

[9] Navidpour, R., Azdast, T., Hasanzadeh, R., Moradian, M., Mihankhah, P., Rasouli, A. Sound-insulation performance of polylactic acid parts 3D printed by fused filament fabrication with functionally graded porous structure for effective noise reduction, Macromol. Mater. Eng. n/a (n.d.) 2400450. https://doi.org/10.1002/mame.202400450.

[10] R. Hasanzadeh, P. Mihankhah, T. Azdast, S. Aghaiee, C.B. Park, Optimization of process parameters of fused filament fabrication of polylactic acid composites reinforced by aluminum using Taguchi approach, Metals (Basel) 13 (6) (2023) 1013, https://doi.org/10.3390/met13061013.

[11] R. Hasanzadeh, P. Mihankhah, T. Azdast, M. Bodaghi, M. Moradi, Process-property relationship in polylactic acid composites reinforced by iron microparticles and 3D printed by fused filament fabrication, Polym. Eng. Sci. 64 (2024) 399–411, https://doi.org/10.1002/pen.26556.

[12] R.T. Mushtaq, Y. Wang, C. Bao, M. Rehman, S. Sharma, A.M. Khan, E.M.-T. Eldin, M. Abbas, Maximizing performance and efficiency in 3D printing of polylactic acid biomaterials: unveiling of microstructural morphology, and implications of process parameters and modeling of the mechanical strength, surface roughness, print time, and print energy for fused filament fabricated (FFF) bioparts, Int. J. Biol. Macromol. 259 (2024) 129201, https://doi.org/10.1016/j.ijbiomac.2024.129201.

[13] B.W. Arifvianto Yuris Bahadur, Urip Agus Salim, Suyitno Suyitno, Muslim Mahardika, Effects of extruder temperatures and raster orientations on mechanical properties of the FFF-processed polylactic-acid (PLA) material, Rapid Prototyp. J. 27 (2021) 1761–1775, https://doi.org/10.1108/rpj-10-2019-0270.

[14] B. Radulescu, A.M. Mihalache, A. Hrituc, M. Radulescu, L. Slatineanu, A. Munteanu, O. Dodun, G. Nagit, Thermal expansion of plastics used for 3D printing, Polymers (Basel) 14 (2022), https://doi.org/10.3390/polym14153061.

[15] B. Tyler, D. Gullotti, A. Mangraviti, T. Utsuki, H. Brem, Polylactic acid (PLA) controlled delivery carriers for biomedical applications, Adv. Drug Deliv. Rev. 107 (2016) 163–175, https://doi.org/10.1016/j.addr.2016.06.018.

[16] S. Aghaiee, T. Azdast, R. Hasanzadeh, F. Farhangpazhouh, Fabrication of bone tissue engineering scaffolds with a hierarchical structure using combination of 3D printing/gas foaming techniques, J. Appl. Polym. Sci. 141 (2024) e55238, https://doi.org/10.1002/app.55238.

[17] H. Lee, D.Y. Shin, Y. Na, G. Han, J. Kim, N. Kim, S.-J. Bang, H.S. Kang, S. Oh, C.-B. Yoon, J. Park, H.-E. Kim, H.-D. Jung, M.-H. Kang, Antibacterial PLA/Mg composite with enhanced mechanical and biological performance for biodegradable orthopedic implants, Biomater. Adv. 152 (2023) 213523, https://doi.org/10.1016/j.bioadv.2023.213523.

[18] H. Lee, D.Y. Shin, S.-J. Bang, G. Han, Y. Na, H.S. Kang, S. Oh, C.-B. Yoon, S. Vijayavenkataraman, J. Song, H.-E. Kim, H.-D. Jung, M.-H. Kang, A strategy for enhancing bioactivity and osseointegration with antibacterial effect by incorporating magnesium in polylactic acid based biodegradable orthopedic implant, Int. J. Biol. Macromol. 254 (2024) 127797, https://doi.org/10.1016/j.ijbiomac.2023.127797.

[19] H. Lee, G. Han, Y. Na, M. Kang, S.-J. Bang, H.S. Kang, T.-S. Jang, J.-H. Park, H. L. Jang, K. Yang, H. Kang, H.-D. Jung, 3D-printed tissue-specific nanospike-based adhesive materials for time-regulated synergistic tumor therapy and tissue regeneration in vivo, Adv. Funct. Mater. 34 (2024) 2406237, https://doi.org/10.1002/adfm.202406237.

[20] S.C. Cox, J.A. Thornby, G.J. Gibbons, M.A. Williams, K.K. Mallick, 3D printing of porous hydroxyapatite scaffolds intended for use in bone tissue engineering applications, Mater. Sci. Eng. C 47 (2015) 237–247, https://doi.org/10.1016/j.msec.2014.11.024.

[21] S. Hassanajili, A. Karami-Pour, A. Oryan, T. Talaei-Khozani, Preparation and characterization of PLA/PCL/HA composite scaffolds using indirect 3D printing for bone tissue engineering, Mater. Sci. Eng. C 104 (2019) 109960, https://doi.org/10.1016/j.msec.2019.109960.

[22] A. Dussault, A.A. Pitaru, M.H. Weber, L. Haglund, D.H. Rosenzweig, I. Villemure, Optimizing design parameters of PLA 3D-printed scaffolds for bone defect repair, Surgeries 3 (2022) 162–174, https://doi.org/10.3390/surgeries3030018.

[23] R. Hasanzadeh, A new polymeric hybrid Auxetic structure additively manufactured by fused filament fabrication 3D printing: machine learning-based energy absorption prediction and optimization, Polymers (Basel) 16 (2024), https://doi.org/10.3390/polym16243565.

[24] K. Elhattab, S.B. Bhaduri, P. Sikder, Influence of fused deposition modelling nozzle temperature on the rheology and mechanical properties of 3D printed B-tricalcium phosphate (TCP)/polylactic acid (PLA) composite, Polymers (Basel) (2022), https://doi.org/10.3390/polym14061222.

[25] H. Zhang, X. Mao, Z. Du, W. Jiang, X. Han, D. Zhao, D. Han, Q. Li, Three dimensional printed macroporous polylactic acid/hydroxyapatite composite scaffolds for promoting bone formation in a critical-size rat calvarial defect model, Sci. Technol. Adv. Mater. (2016), https://doi.org/10.1080/14686996.2016.1145532.

[26] S. Rosso, L. Iannucci, On the compressive response of polymeric cellular materials, Materials 13 (2) (2020) 457, https://doi.org/10.3390/ma13020457.

[27] D.V. Dias Ana C., Eunice Cunha, Maria C. Paiva, Rui L. Reis, Cedryck Vaquette, Natália M. Alves, 3D-printed cryomilled poly(ε-caprolactone)/graphene composite scaffolds for bone tissue regeneration, J Biomed Mater Res B Appl Biomater 109 (2020) 961–972, https://doi.org/10.1002/jbm.b.34761.

[28] R. Roque, G.F. Barbosa, A.C. Guastaldi, Design and 3D bioprinting of interconnected porous scaffolds for bone regeneration. An additive manufacturing approach, J. Manuf. Process. 64 (2021) 655–663, https://doi.org/10.1016/j.jmapro.2021.01.057.

[29] J. Du, Y. Wang, X. Xie, M. Xu, Y. Song, Styrene-assisted maleic anhydride grafted poly(lactic acid) as an effective compatibilizer for wood flour/poly(lactic acid) bio-composites, Polymers (Basel) (2017), https://doi.org/10.3390/polym9110623.

[30] M.S. Barkhad, B. Abu-Jdayil, A.I. Mourad, M. Iqbal, Thermal insulation and mechanical properties of polylactic acid (PLA) at different processing conditions, Polymers (Basel) 12 (9) (2020) 2091, https://doi.org/10.3390/polym12092091.

[31] X. Zhao, Z. Huang, D. Zhang, W. Zhou, S. Peng, High-performance poly(lactic acid)/starch materials prepared via starch surface modification and its in situ enhancement, J. Appl. Polym. Sci. 141 (10) (2023) e55041, https://doi.org/10.1002/app.55041.

[32] S. Vyavahare, S. Kumar, D. Panghal, Experimental study of surface roughness, dimensional accuracy and time of fabrication of parts produced by fused deposition modelling, Rapid Prototyp. J. 26 (2020) 1535–1554, https://doi.org/10.1108/RPJ-12-2019-0315.

[33] A. Dey, N. Yodo, A systematic survey of FDM process parameter optimization and their influence on part characteristics, J. Manuf. Mater. Process. (2019), https://doi.org/10.3390/jmmp3030064.

[34] R. Hasanzadeh, P. Mojaver, T. Azdast, S. Khalilarya, A. Chitsaz, Developing gasification process of polyethylene waste by utilization of response surface methodology as a machine learning technique and multi-objective optimizer approach, Int. J. Hydrog. Energy 48 (2023) 5873–5886, https://doi.org/10.1016/j.ijhydene.2022.11.067.

[35] R. Hasanzadeh, M. Mojaver, T. Azdast, C.B. Park, A novel systematic multi-objective optimization to achieve high-efficiency and low-emission waste polymeric foam gasification using response surface methodology and TOPSIS method, Chem. Eng. J. 430 (2022) 132958, https://doi.org/10.1016/j.cej.2021.132958.

[36] M.A. Fuentes, S. Thakur, F. Wu, M. Misra, S. Gregori, A.K. Mohanty, Study on the 3D printability of poly(3-hydroxybutyrate-co-3-hydroxyvalerate)/poly(lactic acid) blends with chain extender using fused filament fabrication, Sci. Rep. 10 (1) (2020) 11804, https://doi.org/10.1038/s41598-020-68331-5.

[37] R.M. R, V. R, R. S, Experimental analysis on density, micro-hardness, surface roughness and processing time of acrylonitrile butadiene styrene (ABS) through fused deposition modeling (FDM) using box Behnken design (BBD), Mater. Today Commun. 27 (2021) 102353, https://doi.org/10.1016/j.mtcomm.2021.102353.

[38] R.T. Mushtaq, M. Alkahtani, A.M. Khan, M.H. Abidi, Advancements in 3D-printed novel Nylon-6: a Taguchi method for surface quality sustainability and mechanical properties, MACHINES 11 (2023), https://doi.org/10.3390/machines11090885.

[39] ASTM INTERNATIONAL, Standard Test Methods for Flexural Properties of Unreinforced and Reinforced Plastics and Electrical Insulating Materials. D790, Annual Book of ASTM Standards, 2002, pp. 1–12, https://doi.org/10.1520/D0790-10.

[40] B. Ergene, I. Sekeroglu, C. Bolat, B. Yalcin, An experimental investigation on mechanical performances of 3D printed lightweight ABS pipes with different cellular wall thickness, J. Mech. Eng. Sci. 15 (2021) 8169–8177, https://doi.org/10.15282/jmes.15.2.2021.16.0641.

[41] G. Chang, Y. Wang, J. He, Y. Xiong, A graph-based path planning method for additive manufacturing of continuous fiber-reinforced planar thin-walled cellular structures, Rapid Prototyp. J. 29 (2023) 344–353, https://doi.org/10.1108/RPJ-01-2022-0027.

[42] W.S. Barbosa, M.M. Gioia, G.P. Temporao, M.A. Meggiolaro, F.C. Gouvea, Impact of multi-lattice inner structures on FDM PLA 3D printed orthosis using industry 4.0 concepts, Int. J. Interact. Des. Manuf. - IJIDEM 17 (2023) 371–383, https://doi.org/10.1007/s12008-022-00962-6.

[43] J. Yang, X. Chen, Y. Sun, J. Zhang, C. Feng, Y. Wang, K. Wang, L. Bai, Compressive properties of bidirectionally graded lattice structures, Mater. Des. 218 (2022), https://doi.org/10.1016/j.matdes.2022.110683.

[44] B.N. Panda, M. Leite, A. Carvalho, B.B. Biswal, Compressive property characterization of fdm printed cellular structures, in: J.F.S. Gomes, S.A. Meguid (Eds.), M2D2015: Proceedings of the 6th International Conference on Mechanics and Materials in Design, 2015, pp. 545–550.

[45] M. Tyburec, J. Zeman, J. Novak, M. Leps, T. Plachy, R. Poul, Designing modular 3D printed reinforcement of wound composite hollow beams with semidefinite programming, Mater. Des. 183 (2019), https://doi.org/10.1016/j.matdes.2019.108131.

[46] J.D. Kechagias, N. Vidakis, M. Petousis, N. Mountakis, A multi-parametric process evaluation of the mechanical response of PLA in FFF 3D printing, Mater. Manuf. Process. 38 (2023) 941–953.

[47] M. Petousis, N. Vidakis, N. Mountakis, E. Karapidakis, A. Moutsopoulou, Functionality versus sustainability for PLA in MEX 3D printing: the impact of generic process control factors on flexural response and energy efficiency, Polymers (Basel) 15 (2023) 1232.

[48] N. Vidakis, C. David, M. Petousis, D. Sagris, N. Mountakis, A. Moutsopoulou, The effect of six key process control parameters on the surface roughness, dimensional

accuracy, and porosity in material extrusion 3D printing of polylactic acid: prediction models and optimization supported by robust design analysis, Adv. Ind. Manuf. Eng. 5 (2022) 100104.

[49] D. Ahn, J.-H. Kweon, S. Kwon, J. Song, S. Lee, Representation of surface roughness in fused deposition modeling, J. Mater. Process. Technol. 209 (2009) 5593–5600, https://doi.org/10.1016/j.jmatprotec.2009.05.016.

[50] E. Vahabli, S. Rahmati, Application of an RBF neural network for FDM parts' surface roughness prediction for enhancing surface quality, Int. J. Precis. Eng. Manuf. 17 (2016) 1589–1603, https://doi.org/10.1007/s12541-016-0185-7.

[51] J. Hartcher-O'Brien, J. Evers, E. Tempelman, Surface roughness of 3D printed materials: comparing physical measurements and human perception, Mater. Today Commun. 19 (2019) 300–305, https://doi.org/10.1016/j.mtcomm.2019.01.008.

[52] G.S. Sandhu, K.S. Boparai, K.S. Sandhu, Effect of slicing parameters on surface roughness of fused deposition modeling prints, Mater. Today Proc. 48 (2022) 1339–1345, https://doi.org/10.1016/j.matpr.2021.09.047.

[53] M.S. Khan, S.B. Mishra, Minimizing surface roughness of ABS-FDM build parts: an experimental approach, Mater. Today Proc. 26 (2019) 1557–1566, https://doi.org/10.1016/j.matpr.2020.02.320.

[54] R.T. Mushtaq, Y. Wang, M. Rehman, A.M. Khan, C. Bao, S. Sharma, S.M.M. Eldin, M. Abbas, Investigation of the mechanical properties, surface quality, and energy efficiency of a fused filament fabrication for PA6, Rev. Adv. Mater. Sci. 62 (1) (2023) 20220332, https://doi.org/10.1515/rams-2022-0332.

[55] C. Ursini, L. Collini, FDM layering deposition effects on mechanical response of TPU lattice structures, MATERIALS 14 (2021), https://doi.org/10.3390/ma14195645.

[56] B. Ergene, I. Sekeroglu, C. Bolat, B. Yalcin, An experimental investigation on mechanical performances of 3D printed lightweight ABS pipes with different cellular wall thickness, J. Mech. Eng. Sci. 15 (2021) 8169–8177, https://doi.org/10.15282/jmes.15.2.2021.16.0641.

[57] J.J. Netto, M. Sardinha, M. Leite, Influence of the cell size and wall thickness on the compressive behaviour of fused filament fabricated PLA gyroid structures, Mech. Mater. 195 (2024) 105051, https://doi.org/10.1016/j.mechmat.2024.105051.

[58] A. Kumar, L. Collini, C. Ursini, J.-Y. Jeng, Energy absorption and stiffness of thin and thick-walled closed-cell 3D-printed structures fabricated from a hyperelastic soft polymer, Materials 15 (2022), https://doi.org/10.3390/ma15072441.

[59] J. Chen, C. Virrueta, S. Zhang, C. Mao, J. Wang, 4D printing: the spotlight for 3D printed smart materials, Mater. Today 77 (2024) 66–91, https://doi.org/10.1016/j.mattod.2024.06.004.

[60] A. Ghalayaniesfahani, B. Oostenbrink, H. van Kasteren, I. Gibson, M. Mehrpouya, 4D printing of biobased shape memory sandwich structures, Polymer (Guildf.) 307 (2024) 127252, https://doi.org/10.1016/j.polymer.2024.127252.